Tenth International Conference on Computational Fluid Dynamics (ICCFD10), Barcelona, Spain, July 9-13, 2018

ICCFD10-248

An Efficient LES-Acoustic Coupling Method for Sound Generation and High Order Propagation from Jets

M.A. Moratilla-Vega*, Kilian Lackhove**, Johannes Janicka**, H. Xia* and G.J. Page*
Corresponding author: m.a.moratilla-vega@lboro.ac.uk

* Department of Aeronautical and Automotive Engineering
Loughborough University, United Kingdom.

** Fachgebiet für Energie- und Kraftwerkstechnik.
Technische Universität Darmstadt. Germany.

Abstract: The use of a hybrid CFD-CAA method is becoming a standard approach for far-field jet noise prediction, due to its low computational cost compared with a direct compressible prediction. Hybrid CFD-CAA methods require the exchange of information between different codes. For 3D far-field propagation that relies on noise sources information, the amount of data that has to be sent can be enormous, since the size of the meshes is typically of the order of million of elements. Hence, the use of traditional file-based approaches to exchange the data between the codes is limited, as hundreds of terabytes for storing the noise sources can be reached and the scalability of the overall method is limited by the available I/O bandwidth. In this work, a coupling strategy is used in which all the necessary data is exchanged directly in memory by using an open-source library called CWIPI [1]. In addition, it includes an interpolation package that allows the use of different mesh topologies for different codes. The code used for the noise source calculation is a Large Eddy Simulations (LES) code that is use for industry design and academic research [2]. For the acoustic propagation, the solver used is APESolver, part of the high-order open-source code Nektar++ [3]. Encouraging results for combustion noise has been presented by Lackhove et al. [4] with a similar methodology.

1 Introduction

Due to the rapid increase in computational power over the last two decades, high fidelity numerical simulations are becoming a powerful predictive tool, even in complex cases. This is allowing its application for industrial design processes, as well as academic research, with faster and more efficient results than most of the experimental campaigns. Some of those applications involve the modelling of multi-physics problems that require the use of multiple specialised solvers to resolve the huge variety of flow phenomena involved. One of these applications is the flow-acoustic field produced by a high-speed jet.

Noise emission is a major concern of the aviation industry, especially in the vicinity of airports when the aircraft is taking-off or landing. During these two phases, the noise generated by the jet exhaust is one of the main sources of the overall emitted sound. In addition, the plume of the jet can interact with other parts of the aircraft, such as the flaps, creating undesirable tones. Hence, it is crucial to understand how jet noise is generated and propagated in order to reduce it for the future aircraft generations. However, jet noise is essentially a far-field problem, and its prediction using just a direct CFD methodology is still prohibitively expensive for realistic problems. The alternative to direct noise simulations is the use of a hybrid approach in which the computational domain is separated in two regions: a near-field region that contains the noise sources, and a far-field domain that propagates the acoustic field to the far-field observer where the noise is measured. The first is solved using a steady or unsteady CFD method, such as RANS or LES, and the second using an acoustic propagation technique, such as integral methods, linearised euler equations (LEE) or acoustic perturbation equations (APE).

Traditionally, surface integral methods have been the main approach used by the jet noise research community, with a preference of the FWH method over other approaches [5–8]. However, defining a suitable surrounding integral surface in complex installed configurations represents an enormous challenge since it cannot intersect any vortical structure, but it has to be placed as close as possible to the jet plume. Furthermore, by using these type of methods, the information about the acoustic sources is lost and only the noise at single observer locations can be calculated.

The present work proposes an alternative and efficient LES-Acoustic parallel coupling strategy that can be applied to both simple isolated cold and hot jets, as well as more complex and realistic jet-flap interaction problems. The paper is structured as follows. Section 2 describes the governing equations of the LES and Acoustic codes used. In section 3 the numerical methods used for each code are explained. The description of the parallel coupling is included in section 4. Section 5 presents the results obtained for three different cases, i.e. cylinder in a crossflow, rod-airfoil interaction and a jet. Finally, section 6 contains the conclusions and future work.

2 Governing Equations

In a typical hybrid CAA method two different set of governing equations are needed. One is used to obtained the noise sources that comes from the physics of the underlying flow field, whereas the other models the propagation of the acoustic waves. In the current work, the LES flow field is described by the filtered compressible Navier-Stokes equations and the acoustic propagation by the APE. Both types of equations are briefly described in the following subsection.

2.1 Filtered Compressible Navier-Stokes Equations

The filtered Navier-Stokes equations for LES of compressible flows can be written as [9]:

$$\partial_t \overline{\rho} + \partial_j \left(\overline{\rho} \widetilde{u}_j \right) = 0 \tag{1}$$

$$\partial_t \left(\overline{\rho} \widetilde{u}_i \right) + \partial_j \left(\overline{\rho} \widetilde{u}_i \widetilde{u}_j + \overline{p} \delta_{ij} - \widetilde{\tau}_{ij} - \mathcal{T}_{ij} \right) = 0 \tag{2}$$

$$\partial_t \left(\overline{\rho} \widetilde{e} \right) + \partial_j \left(\left(\overline{\rho} \widetilde{e} + \overline{p} \right) \widetilde{u}_j - \widetilde{\tau}_{ij} \widetilde{u}_i + \widetilde{q}_j + \mathcal{L}_j \right) - \widetilde{u}_i \partial_j \mathcal{T}_{ij} \tag{3}$$

where ρ, u_i and p are the density, velocity and pressure. The overline represents the LES filter operation, which commutes with the partial derivatives. The use of the tilde refers to the Favre filter operation defined as $\widetilde{u}_i = \overline{\rho u_i}/\overline{\rho}$. $\widetilde{\tau}_{ij} = 2\mu(\widetilde{S}_{ij} - \widetilde{S}_{kk}\delta_{ij}/3)$; $\widetilde{S}_{ij} = (\partial_j \widetilde{u}_i + \partial_i \widetilde{u}_j)/2$ represents the resolved viscous stress tensor. The heat flux is defined as $\widetilde{q}_j = -\lambda \partial_i \widetilde{T}$ and the temperature $\widetilde{T}$ is calculated from the state equation $\overline{p} = \overline{\rho} R \widetilde{T}$.

The LES filtering operation produces some extra terms in equations 1-3 that are called subgrid-terms [9]. These terms represent the effect of the un-resolved subgrid-scales (SGS) and cannot be directly computed from the resolved field. The terms that are usually kept are the subgrid turbulent stress tensor, $\mathcal{T}_{ij} = \overline{\rho} \widetilde{u}_i \widetilde{u}_j$, and the pressure-velocity subgrid term, $\mathcal{L}_j = -(\overline{p} \widetilde{u}_j - \overline{p u_j}/(\gamma - 1)$ [10]. Since the energy contain in the SGS is not directly dissipated by the LES methods, the addition of a damping model is required. This modelling is still heavily discussed within the LES community, and two different approaches are applied by different research groups. The first approach consists on the use of a model that tries to represent the underlying eddy-viscosity of the SGS. These models always contain a constant or dynamic parameter C_m that tunes the amount of dissipation applied. The other approach is the application of an artificial numerical dissipation that it is implicitly provided by the spatial discretisation of the numerical scheme. This is usually refer as Implicit LES (ILES), and it has proven to give satisfactory results when applied to jet noise problems, as it does not create any SGS turbulent viscosity in the two-dimensional shear layer [11]. However, ILES may create some numerical instabilities that could introduce non-physical, spurious oscillations in the high-frequencies of the simulations. To ensure the stability of the simulation, while avoiding the introduction of excessive SGS dissipation, the present work uses the σ-model [12]. In this SGS model the subgrid-scale viscosity is defined as:

$$\mu_{SGS} = (C_m \Delta)^2 \mathcal{D}_m(\mathbf{u}) \tag{4}$$

with,

$$\mathcal{D}_m = \frac{\sigma_3(\sigma_1 - \sigma_2)(\sigma_2 - \sigma_3)}{\sigma_1^2} \tag{5}$$

where $\sigma_1 \geq \sigma_2 \geq \sigma_3 \geq 0$ are the three singular values of the velocity gradient tensor. The main advantage of this model, over more standard models like Smagorinsky, is the property of automatically vanishing when the resolved simulated flow is either two-dimensional or two-component, which includes the pure shear and solid rotation cases. Besides, it does not generate any subgrid-scale viscosity if the resolved scales are in pure antisymmetric or isotropic contraction/expansion. Another important property of the σ-model is that it has the cubic behaviour near solid boundaries without using any ad-hoc treatment.

2.2 Acoustic Perturbation Equations

The acoustic perturbation equations in their APE-4 form, proposed by Ewert and Schröder [13], can be written as:

$$\partial_t p' + \bar{c}^2 \nabla \cdot \left(\bar{\rho} \mathbf{u}' + \bar{\mathbf{u}} \frac{p'}{\bar{c}^2} \right) = \bar{c}^2 q_c \tag{6}$$

$$\partial_t \mathbf{u}' + \nabla (\bar{\mathbf{u}} \cdot \mathbf{u}') + \nabla \left(\frac{p'}{\bar{\rho}} \right) = \mathbf{q}_m \tag{7}$$

where p', $\mathbf{u}$ are the acoustic pressure and acoustic velocity vector; and the overbar defines time averages quantities. These equations are obtained via a flow decomposition into non-acoustic and acoustic quantities of the non-linear and viscous terms of the Navier-Stokes equations. The filtering ensures that only acoustic modes are propagated. Hence, the APE system presents an advantage over the more traditional Linearised Euler Equations (LEE) which suffer from instabilities due to the inclusion of vortical non-acoustic modes. The left-hand side of equations 6 and 7 represents the propagation of waves in non-uniform mean flows. The right-hand side describes the different sources that are present in any aerodynamic noise generation problem. The source terms, q_c and $\mathbf{q}_m$, are defined as

$$q_c = -\nabla \cdot (\rho' \mathbf{u}')' + \frac{\bar{\rho}}{c_p} \frac{\overline{D} s'}{Dt} \tag{8}$$

$$\mathbf{q}_m = -(\boldsymbol{\omega} \times \mathbf{u})' + T' \nabla \bar{s} - s' \nabla \overline{T} - \left(\frac{\nabla (\mathbf{u}')^2}{2} \right)' + \left(\frac{\nabla \cdot \underline{\tau}}{\rho} \right)' \tag{9}$$

The different source terms can be classified in four different categories. The non-linear terms in the continuity and momentum equations, i.e. $-\nabla \cdot (\rho' \mathbf{u}')'$ and $-(\nabla (\mathbf{u}')^2 /2)'$, heat/entropy related terms, i.e., $\bar{\rho}/c_p \cdot \overline{D} s'/Dt$ and $T' \nabla \bar{s} - s' \nabla \overline{T}$, the viscous term, i.e. $(\nabla \cdot \underline{\tau}/\rho)'$, and the vortical term, known as the Lamb vector, $\mathbf{L}' = -(\boldsymbol{\omega} \times \mathbf{u})'$. In the results presented in this paper, only the Lamb vector is consider as a source term, since it is the major contributor for isothermal applications with strong vortical motions, i.e. shear layers and wakes, as demonstrated in [14, 15].

3 Computational Approach

In the present work, two different solvers are used for the LES-APE coupling. This allows the creation of two different meshes that can be optimised for the near-field, where the noise is generated, and the far-field. In the next subsections each of the numerical solvers is explained in more detail.

3.1 LES

The LES is performed with the in-house code of Rolls-Royce plc., HYDRA [2]. HYDRA is a density-based, cell-vertex, finite volume code used mainly for turbomachinery design. The code is capable of solving arbitrary mesh topologies, which gives a great advantage for the simulation of complex geometries. The calculation of the inviscid flux is based on a second-order Roe type scheme, with the inclusion of a smoothing parameter (ϵ) that acts as a blending between the central and the upwind terms in a similar way as in [16], hence controlling the amount of numerical dissipation. The use of this technique, has demonstrated to give satisfactory results in previous studies [17–19]. The equation of the spatial scheme is:

$$F_{ij} = \frac{1}{2}\left(F(Q_i) + F(Q_j)\right) - \frac{1}{2}\epsilon|A_{ij}|\left(L_j(Q) - L_i(Q)\right) \tag{10}$$

where F represents the inviscid part of the flux, Q is the vector of conserved variables and $L()$ the pseudo-Laplacian. The smoothing parameter varies from a very low value in the central region, to one near the boundaries. This ensures that the numerical dissipation is reduced in the near-field region, and increased near the boundaries to minimise the reflection of the outgoing pressure waves. A typical distribution for jet simulations can be seen in Figure 1. For the temporal discretisation, a second-order, four-stages Runge-Kutta explicit algorithm is employed. The size of the time step is chosen to keep the CFL number around one.

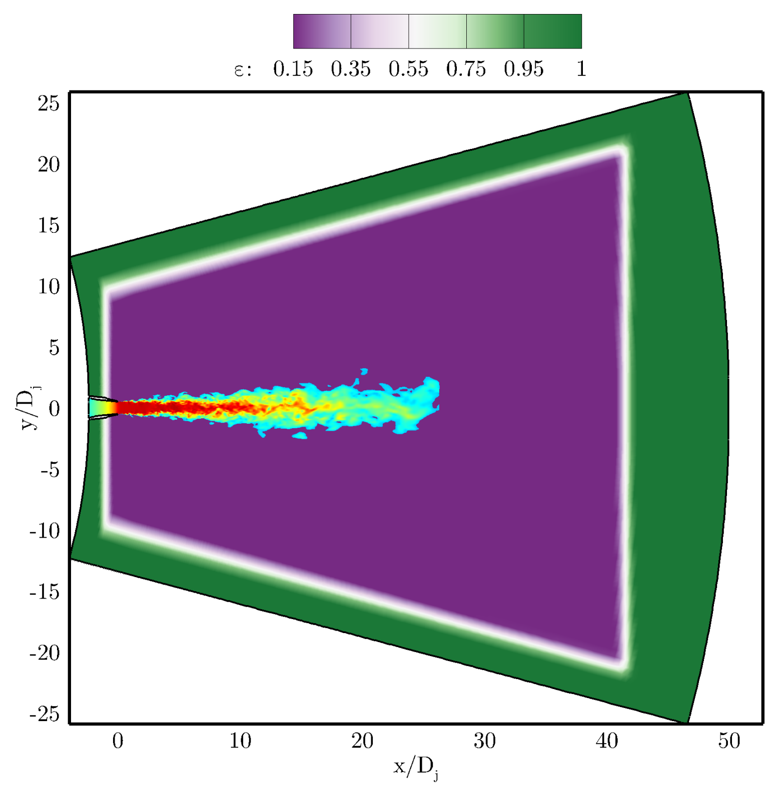

Figure 1: Example of the distribution of ϵ for a jet case.

3.2 APE

The solver used for APE is APESolver, which is part of the open source framework Nektar++ [3]. APESolver solves the APE-4 formulation of the acoustic perturbation equations. The code is a high order, spectral/hp element method with a Discontinuous Galerking (DG) formulation [20]. The DG method uses the variational form of the underlying problem, multiplying the governing system by a test function, and integrating it over the partitioned domain. The solution is then represented locally in each element with a basis of polynomials and a set of quadrature points. In this work the quadrature points are based on a Gauss-Lobatto-Legendre or a modified Legendre basis. Then, the different local elements of the domain are coupled to get the solution of the global problem. The coupling involves the definition of numerical fluxes between adjacent elements. With this method the high spatial resolution required for the propagation of the waves in an efficient way is ensured. The calculation of the fluxes in the APESolver is done with a local Lax-Friderichs scheme as presented in [4]. This equation can be written as:

$$F^R = \frac{1}{2}\left[F(\mathbf{U_L}) + F(\mathbf{U_R}) - |a|_{max}\left(\mathbf{U_R} - \mathbf{U_L}\right)\right] \tag{11}$$

where $|a|_{max}$ is the maximum absolute eigenvalue of the jacobian of F, and $\mathbf{U_L}$ and $\mathbf{U_R}$ the values of the left and right hand side at the interface. The temporal discretisation is performed using a fourth order Runge-Kutta scheme that reduces the dispersion errors. The code incorporates an absorbing forcing condition that is used to damp the amplitude of the outgoing pressure waves, avoiding any reflection at the outer boundaries.

4 Parallel Coupling Mechanism

The coupling procedure is based on the exchange of volumetric, time-dependent data from the LES to the APE application. This means that the amount of information that needs to be exchange between the codes is large, so a more traditional file-based data exchange approach would severely affect the performance of the simulation. On the contrary, exchanging the information on-the-fly, by using an MPI based coupling strategy, significantly improves the efficiency. In addition, the LES and APE use different meshes, that are specifically designed for the noise generation (LES) and the sound propagation steps (APE). Hence, the coupling between the applications also requires the interpolation of the LES source and base-flow data into the APE mesh. Furthermore, since the APE are solved with a spectral/hp, DG method, the higher number of quadrature points has to be considered while performing the interpolation in order to resolve the small scales flow features. However, the minimum element size of the acoustic propagation mesh can be considerably larger than in the LES case, as vortical structures are not resolved by the APE. This allows the use of a greater time step size for the acoustic propagation, which means that the coupling mechanism has to allow for asynchronous communication. A diagram of the parallel coupling strategy is shown in Figure 2, where the low-level interpolation library is an open-source library called CWIPI [1]. CWIPI includes different subroutines/functions that can be added to the applications to exchange the data required, which makes its implementation more complicated than for a file-based strategy. On the other hand, CWIPI provides the capabilities of handling the asynchronous global communication between the applications, and it also contains the possibility of interpolating to an arbitrary number of points within a volumetric cell. This is a feature required to transfer the data between a finite volume and a spectral/hp finite element methods to avoid the generation of spurious sound waves. A more detailed explanation about the implementation of the coupling methodology in Nektar++ can be found in [4].

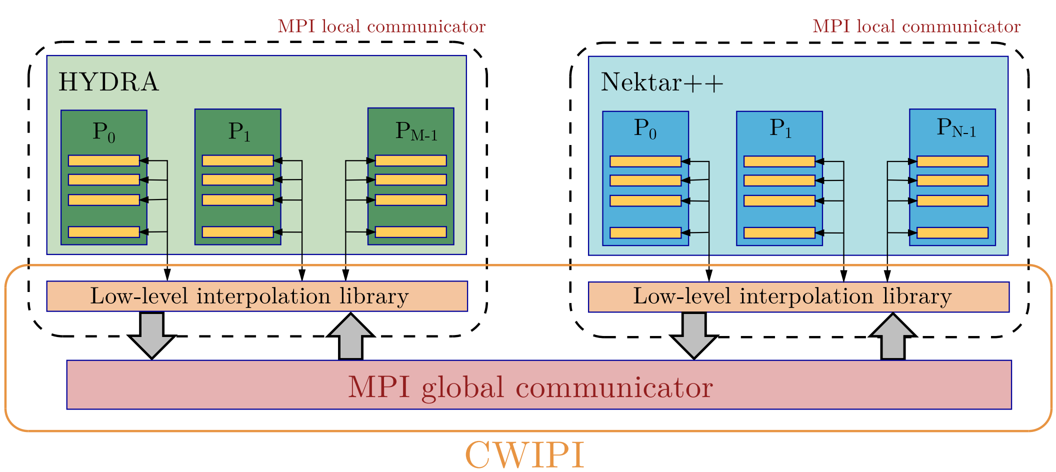

Figure 2: Diagram of the coupling procedure between the LES and the APE codes.

5 Results

This section presents the results obtained for three different cases. First, a 2D cylinder immersed in a M=0.3 and Re=200 flow is used as a validation of the coupling strategy. The fact that only 2D data is required to transfer the sources from the LES to the APE solvers allows to compare the two different coupling methodologies, i.e the more traditional file-based vs the memory-based used in this work. Second, a rod-airfoil interaction case at M=0.2 and Re=48,000 is studied. Finally, a 3D round isothermal turbulent jet at M=0.9 and Re=10,000 is presented.

5.1 Sound Generation of a Cylinder in a Crossflow

A cylinder in a crossflow at Mach number 0.3 and Reynolds number 200 is used as an initial validation for the coupling strategy. In this case, the sound is generated by the vortex shedding created by the cylinder. With the Mach and Reynolds numbers used in the study, one non-dimensionalised period of the shedding is $T/(D_{cyl} \cdot c_\infty) = 17$, which correspond to a non-dimensional wave length of $\lambda/D_{cyl} = 17$. For the compressible simulation, the mesh used is an O-grid that extends radially 80 cylinder diameters and has a resolution of 600×576 points in the circumferential and radial direction respectively, as in [13]. This ensures that the coarsest resolution of the mesh in the circumferential direction contains 22 points per wave length (PPW), which is near the acoustic resolution limit for second-order schemes of 21.3 PPW [21].

The acoustic mesh for the memory-based coupling (APE-Memory) consists on an O-grid with 150×144 points in the circumferential and radial directions. In addition, a Gauss-Lobatto-Legendre basis, fourth-order expansion is applied. With this resolution, the largest element non-dimensional length in the circumferential direction is $h_{max}/D_{cyl} = 10.06$. According to Moura et al. [22] the fourth-order expansion used in this case can resolve, with an error below 1%, non-dimensional wavelengths of $\lambda_{min}/D_{cyl} = 2\pi h_{max}/(D_{cyl} \cdot |kh|_{1\%}) = 10.25$, with $|kh|_{1\%} = 6.164$.

The results obtained with the memory-based coupling are also compared with those of a traditional file-based coupling (APE-File) presented in [23]. However, since the interpolation for the file-based method is based on a cloud of points and an inverse distance algorithm, the use of a coarser mesh with higher polynomial order does not avoid the generation of spurious sound sources. For this reason, the simulation for the file-based approach is carried out in the same mesh as the CFD to avoid any interpolation related issue. The resolution of the two meshes near the cylinder can be seen in Figure 3. It is worth noting that the APE-memory mesh includes the polynomial points created by the high-order expansion.

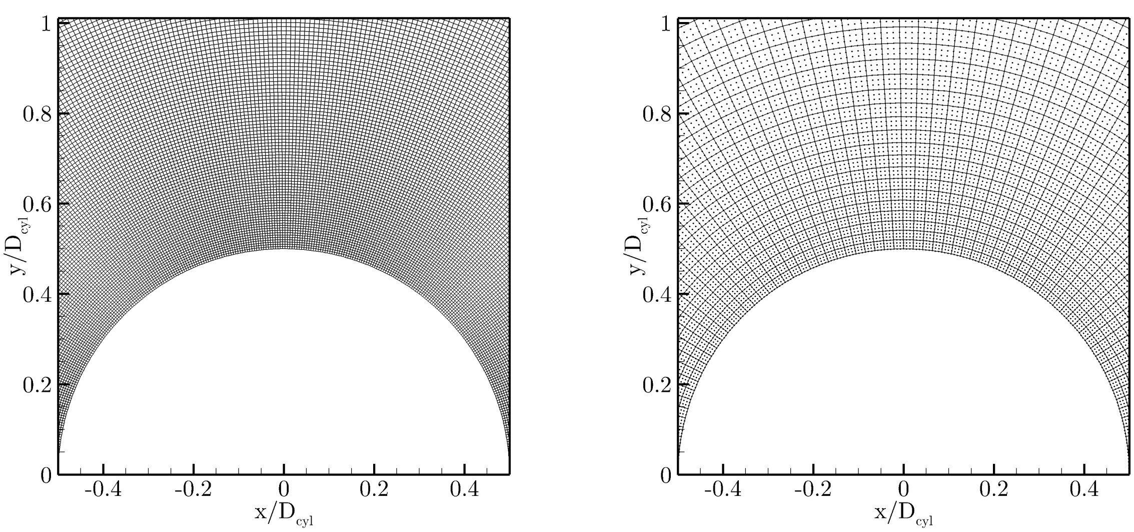

(a) CFD and APE-File

(b) APE-Memory

Figure 3: Mesh resolution of the CFD and the APE cases. The APE-Memory mesh includes the polynomial points.

Figure 4 shows perturbation pressure contours for the three cases. The magnitude and shape of the waves are very similar in the three cases, which demonstrates that the Lamb vector, used in this study as the sole source term, is the most dominant.

The agreement between the cases is further analysed in Figure 5 in which the non-dimensional perturbation pressure distribution is plotted at a constant line along the y-axis at $x = 0$. On the left-hand side figure the second-order highly-resolved CFD and APE-File results are compared with the analytical solution obtained from Curle's analogy [24]. A comparison between the results of the APE-File approach and the coarser third-order APE-Memory approach are shown on the right-hand side figure. Overall, the agreement between the APE results, for both the file and memory approach, with the CFD and analytical solution are encouraging, and demonstrate the capabilities of using this methodology for complex problems.

To show the advantages of using the memory-coupled approach proposed in this work a scalability test has been performed on this case comparing the two types of coupling for the APE propagation code. In order to stablish a fair comparison between the two methods, a few assumptions have been made.

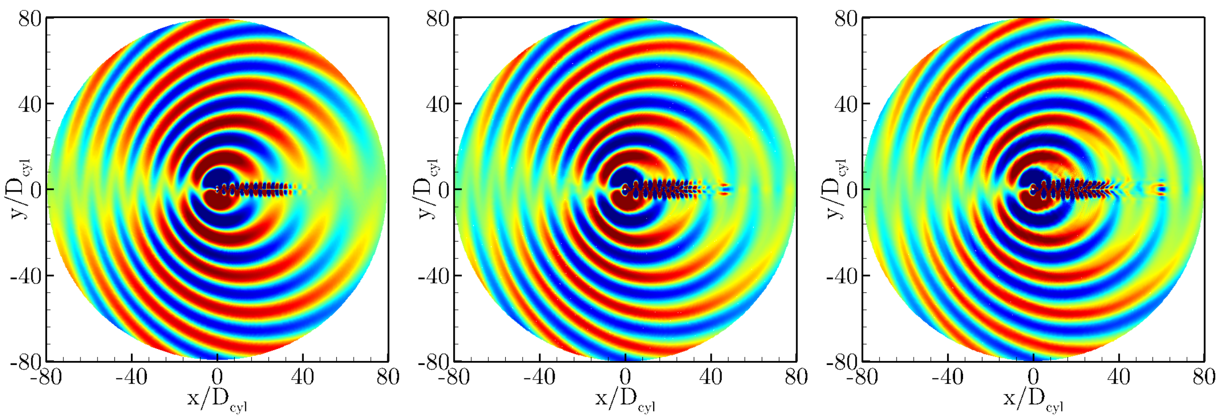

(a) CFD (b) APE-File (c) APE-Memory

Figure 4: Contour of pressure perturbation for the CFD and the CFD-APE simulations. Colourscale from −100 Pa to 100 Pa.

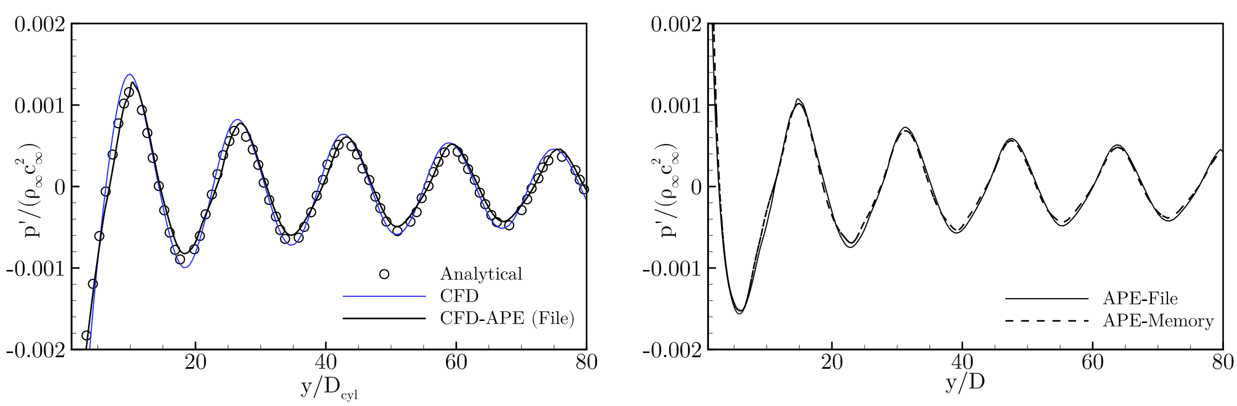

Figure 5: Distribution of pressure perturbation along a perpendicular line at $x = 0$ for the CFD, CFD-APE and Analytical solution (left). Comparison of the pressure perturbation distribution between the APE-File and APE-Memory coupling methods (right).

First, since in the memory-coupled strategy the two codes run simultaneously, the number of processes chosen for the CFD code, HYDRA, are large enough so that the time consumption per time step is of the order of the APE code, avoiding any waiting time between the two codes. Second, for the file-based approach, the increased in the required time due to the writing of the files by HYDRA is neglected in this study. Third, the two coupling types have been tested using the finest grid (APE-File mesh) with a second-order expansion type. In addition, the number of points stored for the file-base coupling has been significantly reduced as only a rectangular area of $x/D_{cyl} = [-1, 40]$ and $r/D_{cyl} = [-5, 5]$ has been considered. This decreases the total number of points to be interpolated from 345,600 to around 150,000. In the memory-coupling case, all the source information of the grid points is send from the CFD to the APE code.

Figure 6 and Table 1 show the results obtained for the three cases studied. The scalability of the APE-Memory case and the standalone APE probe that the coupling method based on a parallel communication interface is incredibly efficient compared to the file-based case. This is due to the bottleneck that the I/O reading speed represents making the performance of the codes dramatically decrease. The I/O bottleneck can be seen in the fact that the time required for reading a file is greater than the time used for advancing the solution when more than 28 processors are used. It is also worth noting that the reading operation of the file-based approach also affects the time required to advance the solution, making the whole running of the APE-File case three times more expensive than the standalone or the APE-Memory, even when only 14 processes are used.

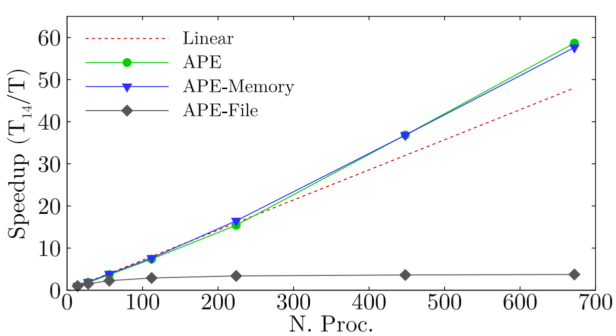

Figure 6: Strong scaling for APE, APE-Memory and APE-File on HPC Midlands.

N. Proc.	APE	APE-Mem.	APE-File
14	1.00	1.00	1.00
28	1.86	1.94	1.54
56	3.69	3.87	2.26
112	7.39	7.61	2.91
224	15.41	16.48	3.4
448	36.84	36.81	3.62
672	58.65	57.61	3.74

Table 1: Parallel speed-up comparison for running standalone and coupled-via-memory and files.

5.2 Rod Wake-Airfoil Interaction

This case is considered a benchmark for CAA codes because of the quasi-tonal and broadband nature that appears in many realistic applications. The computational domain has been created following the dimensions specified by the experimental setup of Jacob et al. [25]. A sketch with the relative dimensions is shown in Figure 7. The setup consists of a rod, with a diameter of $d = 10mm$, and a NACA0012 airfoil, with a chord of $c = 10d$, in tandem configuration. The inflow velocity is $U_\infty = 72m/s$ which gives a Mach number of $M = 0.2$ and a Reynolds number of $Re = 48,000$. This condition generates a vortex shedding frequency in the rod wake of about 1.3 kHz that corresponds to a Strouhal number of $St = fd/U_\infty = 0.19$ [26].

For this case, the CFD and APE run in different grids. The CFD mesh is created by the extrusion of a 2D structured domain. The mesh has a D-shape that extends from $-300d$ to $500d$ in the x-axis, from $-250d$ to $250d$ in the y-axis and from $-1.5d$ to $1.5d$ in the z-axis. The mesh is coarsened towards the outer boundaries, where the ϵ factor of Figure 1 is maximum, creating a damping zone that dissipates the outgoing pressure waves avoiding the generation of spurious noise. It contains 8 Million cells distributed in 10 blocks with 32 cells used in the spanwise direction. Since the aim of this study is the noise generated by the interaction of the rod turbulent wake with the airfoil, the resolution of the near-wall turbulence physics at the boundary layers of the rod and the airfoil is not of extreme importance. Hence, the first cell height on the two boundary layers has a non-dimensional wall distance (y^+) of 70.

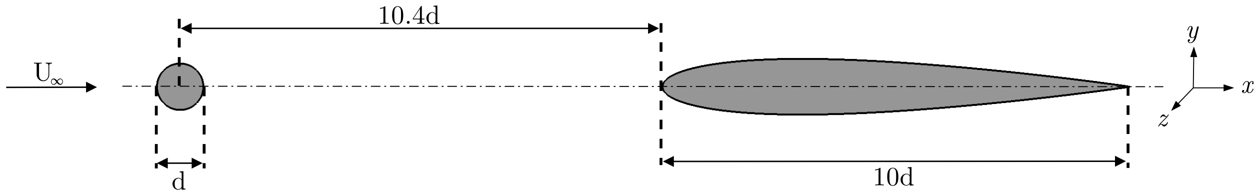

Figure 7: Sketch of the rod-airfoil configuration. The diameter of the rod is given by d. The rest of the measurements are based on d.

The boundaries of the mesh are defined as non-slip for the rod and the airfoil, freestream for the outer boundaries, and a slip condition is applied to the spanwise boundaries as in [26]. The simulation is initialised with a uniform velocity of 72 m/s. A cross-section view of the mesh is shown in Figure 8a.

The acoustic mesh consists on a 2D unstructured squared domain that extends from $-250d$ to $250d$ in the x and y-axis and it has a total number of cells of 20,000. The maximum edge length of the grid is $0.09m$ and a polynomial expansion of fourth-order with a modified-Legendre basis is used. Applying the equation presented in the previous section, the grid at the maximum edge length is capable of resolving wavelengths of $\lambda_{min}/D_{cyl} = 2\pi h_{max}/(D_{cyl} \cdot |kh|_{1\%}) = 0.07m$, which corresponds to a $St = 0.67$. This cut-off frequency is more than three times the shedding frequency of the rod. The near-field mesh is shown in Figure 8b.

The instantaneous spanwise vorticity and velocity fields obtained with the LES computation are mapped in Figure 9. From the two contours it is possible to see the large vortices shed from the rod impinging into the airfoil and being split at the leading edge. In addition, smaller turbulent structures can be seen at the wakes of the rod and the airfoil that contribute to the generation of high frequency noise. The combination of the large vortices, or von Kármán vortices, and the smaller turbulence structures generate the quasi-tonal plus broadband nature of this particular rod-airfoil configuration.

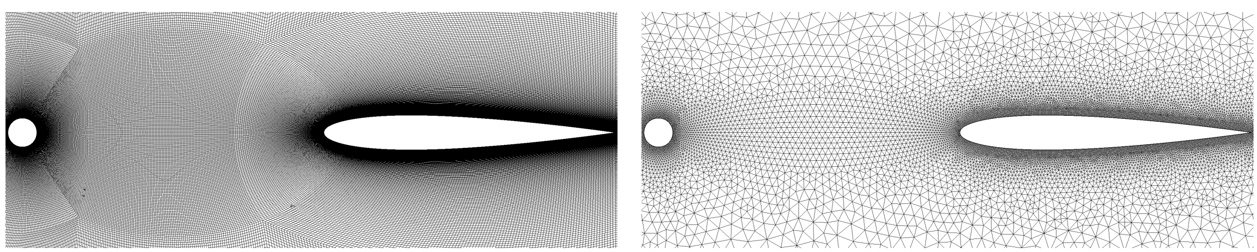

(a) 3D LES Mesh

(b) 2D APE Mesh.

Figure 8: Detail of the LES and the APE mesh used in the rod-airfoil study.

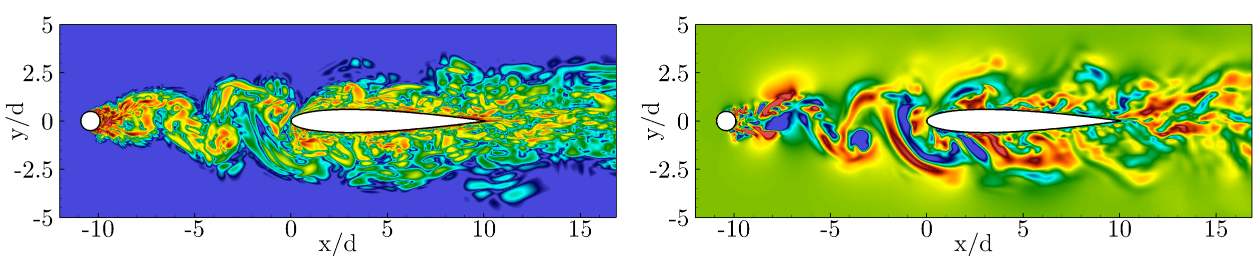

(a) $|\omega_z| = [100, 150 \cdot 10^3]$ $1/s$

(b) $w = [-20, 20]$ m/s

Figure 9: Contours of instantaneous spanwise vorticity and velocity fields.

The results obtained with the LES calculation are compared against the experimental results obtained by Jacob et al. [25]. In particular, mean axial velocity and rms velocity fluctuations are shown in Figure 10 at two different cross-sections. Figure 10a shows the profile obtained at $x/d = -2.55$ which correspond to a location of about $7.5d$ in the far rod wake. There is a good agreement between the present LES and the experimental results, with only a small overprediction near the centre of the wake in terms of mean velocity. In addition, the rms of the axial velocity fluctuation shows that the two shear layers of the LES calculation have merged in a similar way as in the experiment. Figure 10b is dedicated to the profiles at $x/d = 2.5$, which is near the airfoil thickest cross-section. Both the mean velocity and rms velocity fluctuation compare well with the experiment (only 7% overprediction) considering the very coarse near wall resolution of the grid.

For the acoustic propagation, only results with the LES-APE Memory approach have been obtained due to the different grids used for each solver that limits the use of the APE File approach. Probes has been taken at a distance of $x/d = 185d$ and 90° for a total of 200 normalised time units (tU_∞/d). This corresponds to a spectral resolution of 93 Hz, or $St = 0.013$, whereas the spectral resolution of the experiment was 4 Hz, or $St = 5.6 \cdot 10^{-4}$. However, Jacob et al. [25] found that below $St < 0.05$ the noise produce by the wind tunnel was dominant, so any measurement below that Strouhal number is neglected in this study.

Due to the use of a 2D mesh for the acoustic propagation, and a reduced spanwise grid for the LES calculation, two correction factors are required in order to compare the results obtained with the present methodology against the experiment. The corrections used in this work are Oberai's correction [27], that relates the 2D with the 3D radiated sound, and Kato's correction [28] to account for the span difference between the simulation and the experiment. The effect of the corrections on the PSD follows:

$$PSD|_{3D} = PSD|_{2D} + 10\log\left(\frac{\omega \cdot L_s^2}{c_\infty \pi R}\right) + 10\log\left[\sum_{i=1}^{N}\sum_{j=1}^{N}\exp\left(-(i-j)^2\left(\frac{L_s}{L_c(\omega)}\right)^2\right)\right] \tag{12}$$

where ω is the frequency, L_s the simulated model span length, R the distance to the observer point, $N = 10$ is the number of simulated lengths that are required to match the span length of the experiment, and $L_c(\omega)$ the spanwise coherence length. In this work the spanwise coherence length has been taken from Jacob's experiment [25].

The results obtained are presented in Figure 11. Figure 11 left shows a contour of the pressure perturbation resolved with the APE calculation. A tonal noise component is clearly distinguishable that radiates from the rod wake-airfoil interaction to the far-field. The power spectral density (PSD) results obtained for the observer point $x/d = 185d$ and 90°, Figure 11 right, show an accurate prediction of the LES-APE calculation compared to the experiment. Moreover, the peak is correctly captured with a small underprediction of 3dB.

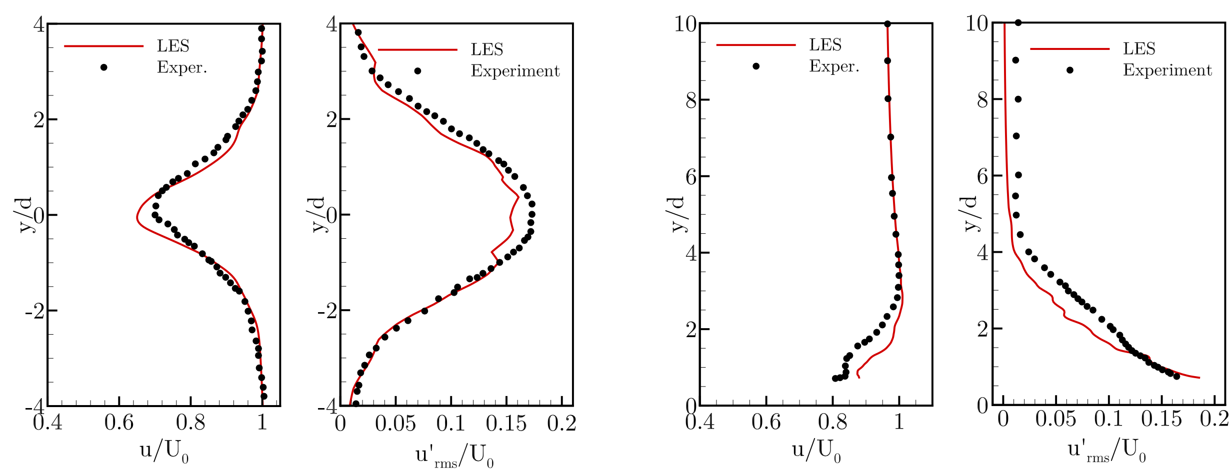

(a) $x/d = -2.55$ (b) $x/d = 2.50$

Figure 10: Axial velocity and Reynolds stress profiles of LES and experiment [25].

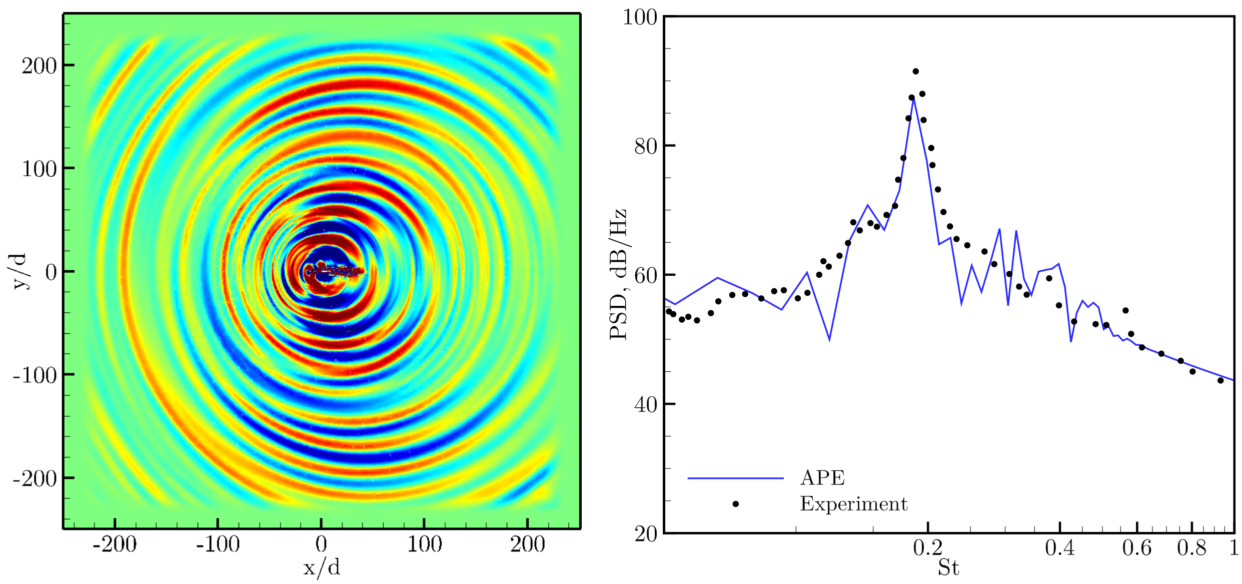

Figure 11: Contours of pressure perturbation (left) and power spectral density for an observer at $x/d = 185$ and 90°(right). Colourscale from -100 to 100 Pa. Comparison with experiment [25].

5.3 Jet Noise

A 3D turbulent isothermal jet at Mach $M = 0.9$ and Reynolds number $Re = 10,000$ is simulated to verify the capabilities of the present methodology for complex 3D cases. As in the previous study two different multi-block meshes have been used . In both cases the mesh is created using only hexaedral elements. The computational LES domain is similar to the one presented by Shur et. al [5], with the inclusion of the outer wall of the nozzle for a better prediction of the noise at upstream angles. The LES domain extends from $x/D_j = [-5, 100]$ and from $y/D_j = [-50, 50]$ and it has a cylindrical shape. The mesh is form of 190 $\times$ 75 $\times$ 49 nodes in the axial, radial and azimuthal directions respectively, giving a total number of 630,000 elements. As in the rod-airfoil case, the grid is coarsened near the outer boundaries to dissipate the outgoing pressure waves with the addition of the increase numerical dissipation factor ϵ. The mesh is refined near the nozzle to better capturing the initial shear layer development. The inlet boundary condition is a laminar total pressure profile.

The acoustic propagation domain has a cubical shape to get a more uniform distribution of the hexaedral elements in the three spacial directions, avoiding a significantly different spacial resolution in the y and z directions. The grid is generated using 108 $\times$ 70 $\times$ 70 points in the x, y and z directions respectively, and it has around 600,000 elements. The expansion type chosen for this case is a fifth-order Gauss-Lobatto-Legendre basis. Since the size of the maximum element is around $h_{max}/D_j = 2$ the spacial resolution of this mesh can resolve frequencies up to a Strouhal number of $St = 1$ with less than 1% error [22]. The mesh extends from -5 to 40 jet diameters in the x direction, and from -25 to 25 jet diameters in the y and z directions. An absorption layer of $3D_j$ is defined near the outer boundaries to avoid any reflection of the outgoing waves. The use of a much coarser mesh near the nozzle exit allows an increase by a factor of 3 of the time step size compared to the compressible LES.

Figure 13 shows vorticity magnitude contours of a z-plane and a x-plane cuts at 0 and 1.5 diameters, respectively. The transition from laminar to turbulent regime occurs at around 1.5 diameters from the nozzle, as the x-plane cut shows. This means that coherent structures may be found in the first 1.5 diameters, which could affect the propagated noise, creating spurious tones. Figure 14 displays centreline mean axial velocity and rms axial velocity fluctuations results compared with the high-order LES study of Shur et al. [5] and the experiment of Stromberg [29]. The present LES is in good agreement with [5, 29]. There is a small overprediction of the rms axial velocity fluctuation values that could be caused by the use of a second-order scheme in a coarse mesh, as explained in [5]. However, the maximum peak value and location is well captured by the present LES, which means that the development of the shear layer is similar to Shur et al. results.

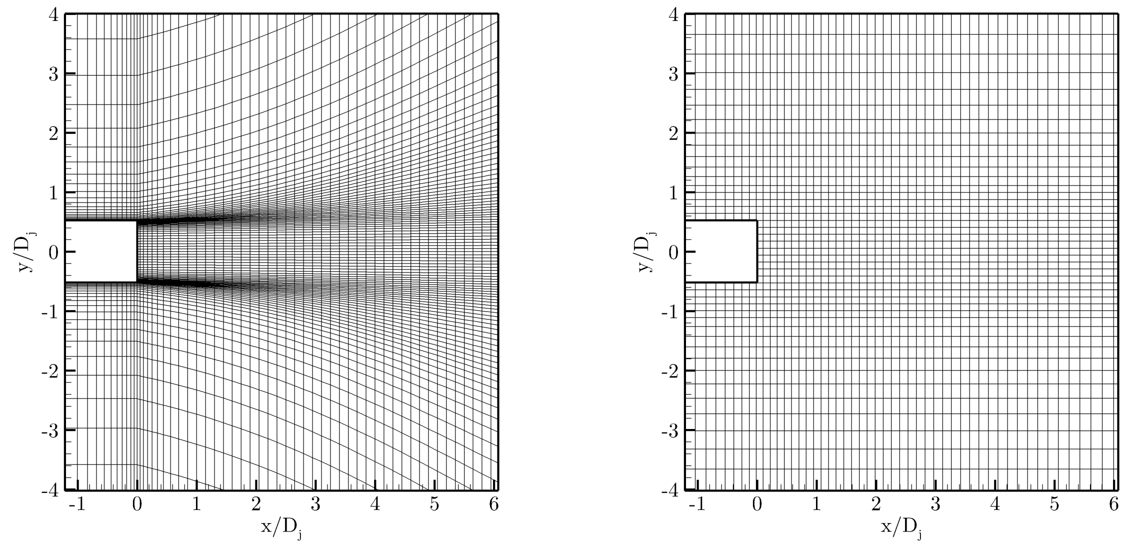

(a) LES Mesh (b) APE Mesh

Figure 12: Cross-sections of the LES and the APE meshes used in the jet noise calculations.

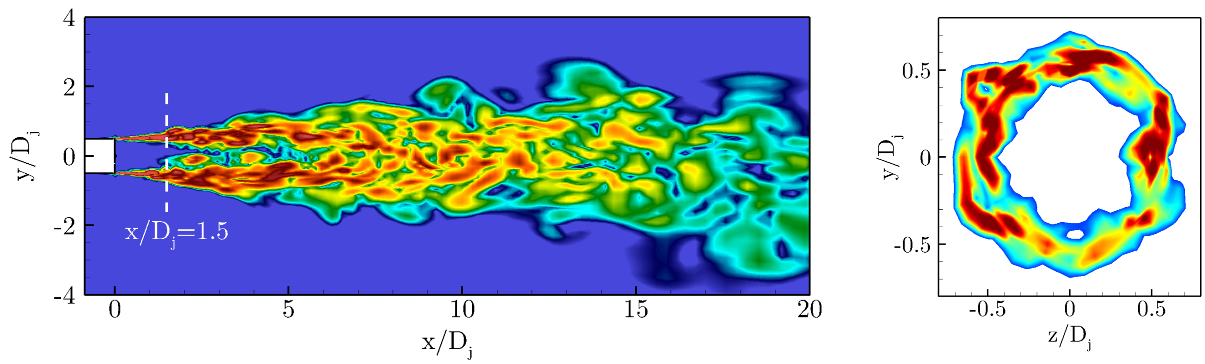

Figure 13: Contours of vorticity magnitude for a z-plane and a x-plane cuts at $z/D_j = 0$ and $x/D_j = 1.5$, respectively. Colorscale from 30 to 3000 $1/s$.

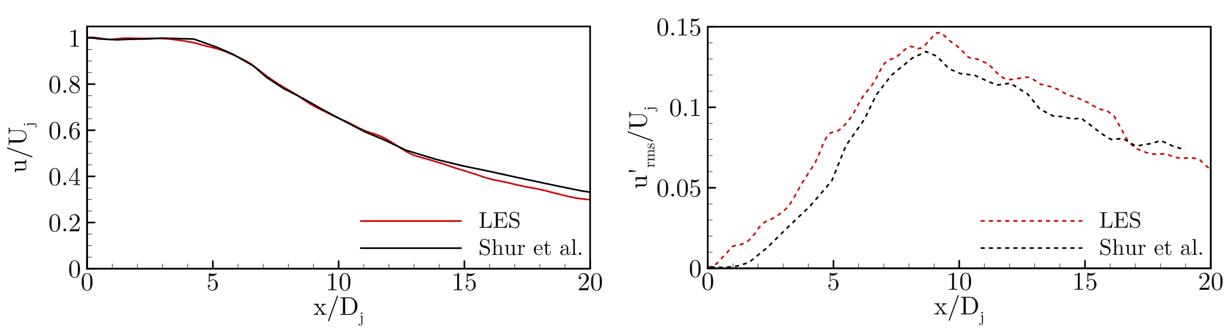

Figure 14: Centreline mean axial velocity and rms axial velocity fluctuations. Comparison with LES from [5].

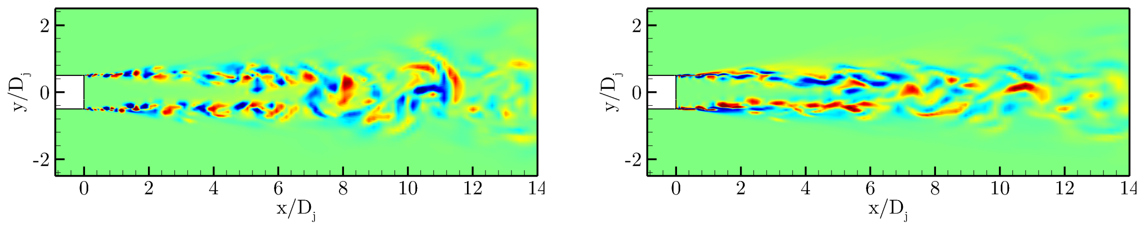

Figure 15: Contours of the first two components of the Lamb vector perturbation $\mathbf{L}' = -(\boldsymbol{\omega} \times \mathbf{u})'|_{x,y}$. Colourscale from -10^8 to 10^8 (left) and $-4 \cdot 10^8$ to $4 \cdot 10^8$ (right).

In addition to the instantaneous and mean velocity values, the fluctuation of the first two components of the Lamb vector is presented for this case in Figure 15. The calculation of the Lamb vector fluctuations follows the equation:

$$\mathbf{L}' = -(\boldsymbol{\omega} \times \mathbf{u})' = -(\boldsymbol{\omega} \times \mathbf{u}) + \overline{(\boldsymbol{\omega} \times \mathbf{u})} \tag{13}$$

where the mean part of the Lamb vector is stored during the average run of the LES. Since the jet mesh is axisymmetric, an azimuthal average of the mean Lamb vector is performed. The contours further confirm the assumption of coherent sources being generated in the first 1.5 diameters as symmetric noise sources can be seen at the top and the bottom shear layers. After two diameters the symmetry disappears, which is an indicator of the flow being in the turbulent regime.

For the prediction of the noise in the far-field, FWH and coupled LES-APE calculations have been performed. The FWH calculation [30] is based on a surface that encloses the jet. The FWH surface is long enough to include all the noise sources, which makes possible the omission of the volume quadrupole integral. The FWH surface has been placed following the suggestions of Shur et al. [5] and Di Francescantonio [31]. The integral equation is:

$$4\pi p' = \frac{\partial}{\partial t}\int_S \left[\frac{\rho u_n}{r}\right] dS + \frac{1}{c_\infty}\frac{\partial}{\partial t}\int_S \left[\frac{p'_{nr} + \rho u_n u_r}{r}\right] dS + \int_S \left[\frac{p'_{nr} + \rho u_n u_r}{r^2}\right] dS \tag{14}$$

where r defines the observer position, and S is the FWH surface. The quantities in square brackets are calculated at retarded times. The surface data is stored during the averaging run calculation for 200 normalised time units (tU_∞/D_j). The FWH code used in the present work has already been used in previous studies with satisfactory results [16, 18, 19].

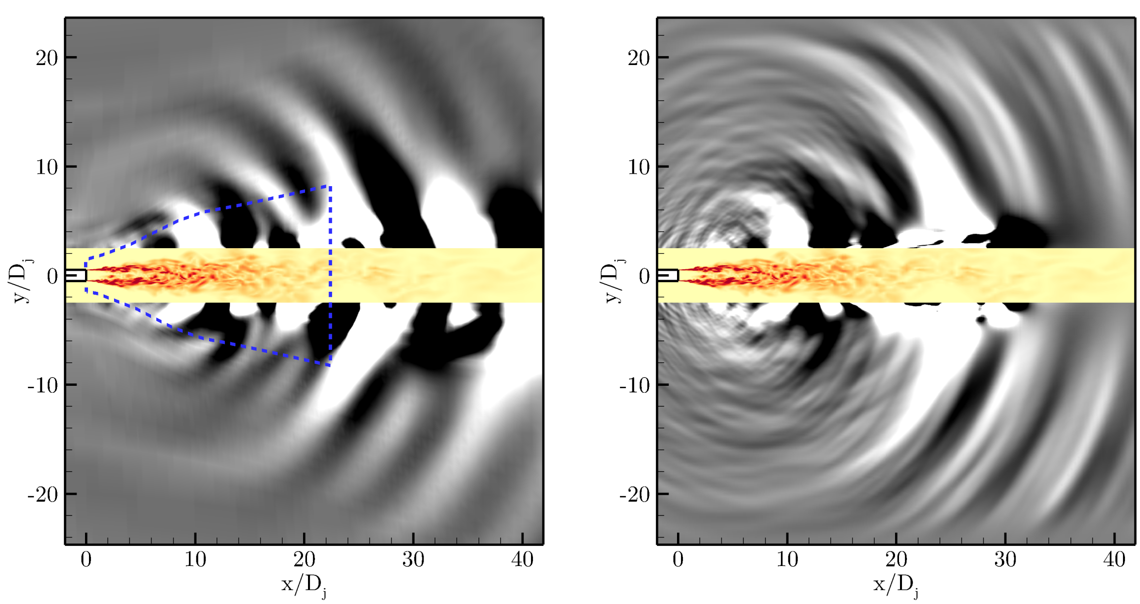

Figure 16: Contours of pressure perturbation for the LES with FWH surface location in blue (left) and APE (right) with vorticity magnitude superposed. Colourscale from -30 to 30 Pa.

For the LES-APE coupled calculation a technique called silent embedded boundaries [32] is used in order to minimise the effect of the coherent vortices in the sound propagation. The method consists in the application of a damping zone of finite thickness near the nozzle boundary. In this case the source damping region is defined from $x = [0, 1.5]$ diameters since the flow exhibits a laminar behaviour in that region. In addition, the sources are smoothly damped from $x = 35D_j$ to avoid their interaction with the outer boundary. Numerical probes are stored at a location of $r = 20D_j$ for a total of 100 normalised time units.

Figure 16 visualises the pressure fluctuation for the LES and the LES-APE coupled calculations at the same time instant. This allows a direct comparison between the waves present in both simulations. It is clear from the contours that the noise content of the APE calculation is much higher than the LES, which is too dissipative due to the low order of the scheme. It is important to mention that, even tough the number of elements, and the edge size, in the two meshes is similar in the propagation region, the polynomial expansion used in the APE calculation gives a much higher spatial resolution than the LES. However, even in areas very close to the nozzle, where the two meshes have the same spatial resolution, high frequency waves are only present in the APE contour.

In Figure 17, the overall sound pressure level (OASPL), and the power spectral density for two observer angles are shown (PSD). The results for the OASPL are compared to the experiments of Tanna [33] ($M = 0.9$, $Re = 10^6$), and Stromberg et al. [29] ($M = 0.9$, $Re = 3,600$). All the results have been scaled to $120D_j$ using the $1/r^2$ rule and have been averaged using 12 azimuthal points. In terms of OASPL the present FWH and APE simulations are quite similar to Stromberg results, which are for a slightly lower Reynolds number, for high angles. This can be an evidence that the numerical dissipation of the present LES is too high due to the coarse mesh that has been used. Hence, the real Reynolds number of the simulation may be lower than 10,000. For low angles the results compared well to both experiments. On the other hand, the PSD level at both 30° and 90° observer points is in good agreement with Tanna's experiment up to a $St = 0.5$. In addition, the cut-off frequency of the APE simulation is almost twice for the 90° which is the location where higher frequencies are more important. This means that although the LES calculation can capture noise sources up to $St = 1$, the high frequency content is already lost when the flow reaches the FWH surface due to the high dissipation of the second-order LES.

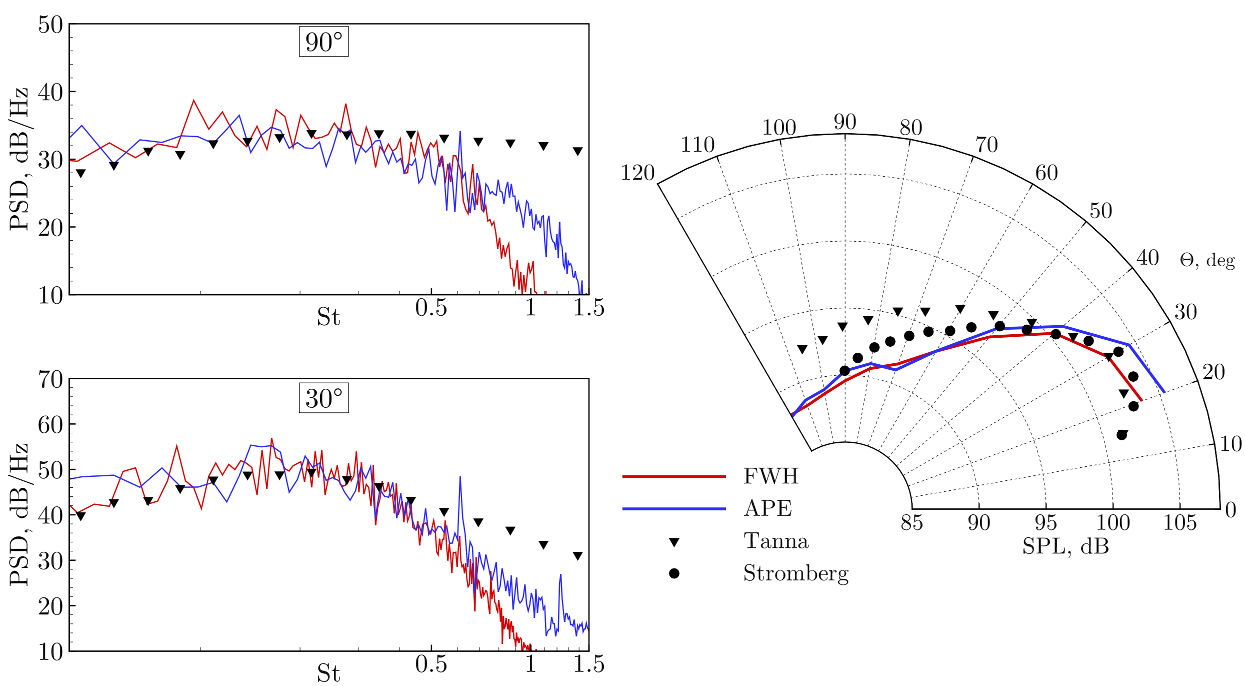

Figure 17: OASPL and PSD results for observers at 30° and 90° at $120D_j$. Comparison with experiments by [29, 33].

6 Conclusion

An LES-APE coupling strategy for the prediction of noise in jets and other configurations has been presented. The method couples an LES second-order code with a high-order spectral APE code in a very efficient way so that it can be used in 3D complex applications. The efficiency of the coupling technique has been tested and compared against the standalone APE code and a traditional file-based coupling approach that was presented in [23]. The scalability test shows encouraging results as the overhead time of the coupling approach is minimum. However, the test was only performed in a 2D case and further scalability studies for 3D applications are required.

The LES-APE methodology is also tested for two configurations that are related to the installed jet problem. First, a rod-airfoil interaction case is presented giving the expected noise prediction when compared with the experiment. It also demonstrates the possibility of using unstructured meshes when complex geometries are involved.

Finally, a 3D turbulent jet case at Re=10,0000 is studied. Both the mean flow statistics and the noise prediction compared well with other groups studies and experiments. Furthermore, it has been shown that the actual methodology could potentially give a higher cut-off frequency prediction when compared to a more traditional FWH approach.

As for future cases a higher Reynolds turbulent jet is currently under study, while installed jet-wing cases are expected to be examined thereafter.

7 Acknowledgment

The authors would like to thank EPSRC for the computational time made available on the UK supercomputing facility ARCHER via the UK Turbulence Consortium (EP/L000261/1). This work was partially funded under the embedded CSE programme of the ARCHER UK National Supercomputing Service. The first author would also like to acknowledge the support given by the HPC at Loughborough University.

References

[1] A. Refloch, B. Courbet, A. Murrone, P. Villedieu, C. Laurent, P. Gilbank, J. Troyes, L. Tessé, G. Chaineray, J.B. Dargaud, E. Quémerais, and F. Vuillot. CEDRE Software. Technical report, AerospaceLab, 2011.

[2] P. Moinier. *Algorithm developments for an unstructured viscous flow solver.* PhD thesis, Oxford University, 1999.

[3] C.D. Cantwell, D. Moxey, A. Comerford, A. Bolis, G. Rocco, G. Mengaldo, D. De Grazia, S. Yakovlev, J.-E. Lombard, D. Ekelschot, and et al. Nektar++: An open-source spectral/hp element framework. *Computer Physics Communications*, 192:205–219, Jul 2015.

[4] K. Lackhove, A. Sadiki, and J. Janicka. Efficient three dimensional time-domain combustion noise simulation of a premixed flame using acoustic perturbation equations and incompressible les. In *ASME Turbo Expo 2017: Turbomachinery Technical Conference and Exposition*, pages V02CT43A001–V02CT43A001. American Society of Mechanical Engineers, 2017.

[5] ML Shur, PR Spalart, M Kh Strelets, and AK Travin. Towards the prediction of noise from jet engines. *International Journal of Heat and Fluid Flow*, 24(4):551–561, 2003.

[6] P.R. Spalart and M.L. Shur. Variants of the Ffowcs Williams-Hawkings equation and their coupling with simulations of hot jets. *International journal of aeroacoustics*, 8(5):477–491, 2009.

[7] S. Mendez, M. Shoeybi, S.K. Lele, and P. Moin. On the use of the Ffowcs Williams-Hawkings equation to predict far-field jet noise from large-eddy simulations. *International Journal of Aeroacoustics*, 12(1):1–20, 2013.

[8] H. Xia, S. Karabasov, O. Graham, P.G. Tucker, A.P. Dowling, K. Depuru, and T.P. Hynes. Hybrid RANS-LES modeling of chevron nozzles with prediction of far field sound. *AIAA Paper*, 21:2011, 2011.

[9] B. Vreman, B. Geurts, and H. Kuerten. Subgrid-modelling in les of compressible flow. *Applied scientific research*, 54(3):191–203, 1995.

[10] C. Bogey and C. Bailly. Computation of a high reynolds number jet and its radiated noise using large eddy simulation based on explicit filtering. *Computers & fluids*, 35(10):1344–1358, 2006.

[11] F. Grinstein and C. Fureby. Recent progress on miles for high reynolds number flows. *Journal of Fluids Engineering*, 124(4):848–861, 2002.

[12] F. Nicoud, H.B. Toda, O. Cabrit, S. Bose, and J. Lee. Using singular values to build a subgrid-scale model for large eddy simulations. *Physics of Fluids (1994-present)*, 23(8):085106, 2011.

[13] R. Ewert and W. Schröder. Acoustic perturbation equations based on flow decomposition via source filtering. *Journal of Computational Physics*, 188(2):365–398, Jul 2003.

[14] E. Gröschel, W. Schröder, P. Renze, M. Meinke, and P. Comte. Noise prediction for a turbulent jet using different hybrid methods. *Computers & Fluids*, 37(4):414?426, May 2008.

[15] R Ewert and W Schröder. On the simulation of trailing edge noise with a hybrid les/ape method. *Journal of Sound and Vibration*, 270(3):509–524, 2004.

[16] H. Xia, P.G. Tucker, and S. Eastwood. Large-eddy simulations of chevron jet flows with noise predictions. *International Journal of Heat and Fluid Flow*, 30(6):1067–1079, 2009.

[17] M. Angelino, M. Moratilla-Vega, H. Xia, and G.J. Page. Large-eddy simulations of high Reynolds number jets with a suitable subgrid-scale model for solver dependency study. *ETMM11 Conference*, 2016.

[18] M. Angelino, H. Xia, M. Moratilla-Vega, and G.J. Page. Far-field Noise Prediction of Round and Serrated Jets with Increasingly Refined Grids. *22nd AIAA/CEAS Aeroacoustics Conference*, May 2016.

[19] M. Mahak, M. Moratilla-Vega, G.J. Page, and H. Xia. Assessment of WALE and Sigma Sub-Grid Scale Models for Jet Noise Prediction. *22nd AIAA/CEAS Aeroacoustics Conference*, May 2016.

[20] G. Karniadakis and S. Sherwin. *Spectral/hp element methods for computational fluid dynamics*. Oxford University Press, 2013.

[21] C. Bailly and D. Juve. Numerical solution of acoustic propagation problems using linearized euler equations. *AIAA journal*, 38(1):22–29, 2000.

[22] R.C. Moura, S.J. Sherwin, and J. Peiró. Linear dispersion–diffusion analysis and its application to under-resolved turbulence simulations using discontinuous galerkin spectral/hp methods. *Journal of Computational Physics*, 298:695–710, 2015.

[23] M. Moratilla-Vega, H. Xia, and G.J. Page. A Coupled LES-APE Approach for Jet Noise Prediction. *46th INTER-NOISE Conference*, August 2017.

[24] N. Curle. The influence of solid boundaries upon aerodynamic sound. *Proc. R. Soc. Lond. A*, 231(1187):505–514, 1955.

[25] M.C. Jacob, J. Boudet, D. Casalino, and M. Michard. A rod-airfoil experiment as a benchmark for broadband noise modeling. *Theoretical and Computational Fluid Dynamics*, 19(3):171–196, 2005.

[26] J. Boudet, N. Grosjean, and M.C. Jacob. Wake-airfoil interaction as broadband noise source: a large-eddy simulation study. *International Journal of Aeroacoustics*, 4(1):93–115, 2005.

[27] A.A Oberai, F. Roknaldin, and T.J. Hughes. Computation of trailing-edge noise due to turbulent flow over an airfoil. *AIAA journal*, 40(11):2206–2216, 2002.

[28] C. Kato, A. Iida, Y. Takano, H. Fujita, and M. Ikegawa. Numerical prediction of aerodynamic noise radiated from low mach number turbulent wake. In *31st Aerospace Sciences Meeting*, page 145, 1993.

[29] J.L. Stromberg, D.K. McLaughlin, and T.R. Troutt. Flow field and acoustic properties of a mach number 0· 9 jet at a low reynolds number. *Journal of sound and vibration*, 72(2):159–176, 1980.

[30] J.E. Ffowcs Williams and D. L. Hawkings. Sound generation by turbulence and surfaces in arbitrary motion. *Phil. Trans. R. Soc. Lond. A*, 264(1151):321–342, 1969.

[31] P. Di Francescantonio. A new boundary integral formulation for the prediction of sound radiation. *Journal of Sound and Vibration*, 202(4):491–509, 1997.

[32] C. Wagner, T. Hüttl, and P. Sagaut. *Large-eddy simulation for acoustics*, volume 20. Cambridge University Press, 2007.

[33] H.K. Tanna. An experimental study of jet noise part i: Turbulent mixing noise. *Journal of sound and Vibration*, 50(3):405–428, 1977.